Trans. Japan Soc. Aero. Space Sci.
Vol. 52, No. 178, pp. 206–212, 2010

Energy Separation in High Subsonic Turbine Cascade

By Mahmoud M. EL-GENDI,[1)] Mohammed K. IBRAHIM,[1),2)] Koichi MORI[1)] and Yoshiaki NAKAMURA[1)]

[1)]*Department of Aerospace Engineering, Nagoya University, Nagoya, Japan*
[2)]*Aerospace Engineering Department, Faculty of Engineering, University of Cairo, Giza, Egypt*

(Received October 31st, 2008)

Trailing edge vortex shedding from a turbine cascade was numerically simulated for an exit isentropic Mach number of 0.79 and a Reynolds number of 2.8×10^6. The objective of this study is to clarify the time evolution of the vortex shedding process from a turbine blade and the mechanism of energy separation appearing in the wake. Calculations used a locally developed numerical code, employing a second-order AUSM scheme for inviscid numerical fluxes, a second-order implicit dual time method for time integration, and Detached Eddy Simulation for turbulence. Calculated results confirmed a non-uniform pressure distribution along the trailing edge, which was observed experimentally and different from a uniform distribution at low subsonic Mach number. The energy separation where instantaneous total temperature splits into hot and cold spots in the wake is caused by convection and vortex rotation. In addition, the formation and dissipation phases of vortices affect the energy separation.

Key Words: Turbine Flows, CFD, Wake, Vortex Shedding, Compressible Flows

1. Introduction

The turbomachinery industry is so global that any small improvement in turbine efficiency and better understanding of flow physics will result in huge benefits. There are several kinds of loss in turbines. The trailing edge loss caused mainly by vortex shedding accounts for more than a third of the total loss.[1)] Kurosaka et al.[2)] proved that vortex shedding causes energy separation by matching the vortex shedding frequency with the wind-tunnel acoustic wave frequency. The energy separation where total temperature instantaneously splits into hot and cold spots is known as the Eckert-Weise effect in the time-average basis. It affects flow uniformity in the stator-rotor interaction, and inlet flow to next stage in multistage turbines. Since, the main purpose of turbines is to extract energy from the flow and convert it to mechanical energy, this effect must be taken into account in design.

In a turbomachine wake, this phenomenon was observed by Carscallen et al.[3)] and confirmed by Sieverding et al.[4)] In a cylinder wake, Goldstein and Kulkarni[5)] observed it at low Mach number where it extends up to ten diameters downstream. Goldstein and He[6)] noticed that when the vortex shedding frequency is locked in to the natural frequency of the wind-tunnel acoustics their amplitudes are increased and the energy separation becomes stronger. Ng and Chakroun[7)] showed that the total pressure has a similar trend to the total temperature. Eckert[8)] analyzed flow conditions where, energy separations can occur and Eckert[9)] reviewed cases where, energy separation occurred. O'Callaghan and Kurosaka[10)] observed it in the wake of screen and flat plat, and Oudheusden[11)] observed it in the afterbody wake at supersonic flow.

In addition to energy, when vortex shedding frequency is locked to a turbomachine frequency, the possibility of blade fatigue and noise increases. A decade ago, Cicatelli and Sieverding[12)] advocated that vortex shedding evolution needs more investigation. Regarding this issue, Desse[13)] conducted an experiment for flat plates, and Cicatelli and Sieverding[14)] considered a turbine cascade with $M_{2,is} = 0.4$. Sondak and Dorney[15)] and Cicalelli et al.[16)] investigated this problem numerically using the same cascade and flow conditions as Cicatelli and Sieverding.[14)] Sieverding et al.[4,17)] conducted experiments at $M_{2,is} = 0.79$ on a blade with half the scale used in other research.[14–16,18)]

This study conducted numerical simulation of trailing edge vortex shedding from a turbine cascade at high subsonic Mach number. Previously, most flow modeling has been limited to the low Mach number case of $M_{2,is} = 0.4$.[15,16)] Experimental results of Sieverding et al.[4,17)] are used to validate our simulated results.

In addition, most previous vortex shedding has been modeled using simple algebraic turbulence models, which are unsuitable for unsteady flows.[15,16,19)] This study uses Detached Eddy Simulation (DES).

Finally, based on our simulation results, we propose a simple explanation for the mechanism of energy separation.

2. Numerical Method

2.1. Model in study

The turbine cascade and flow conditions are the same as those used by Sieverding et al.[4,17)] The VKI blade profile, cascade configuration, computational domain, and cascade dimensions are shown in Fig. 1. The cascade has a chord length (C) of 140 mm, an axial chord (C_{ax}) of 91.84 mm, a pitch (S) of 97.44 mm, and a stagger angle (λ) of 49.83°.

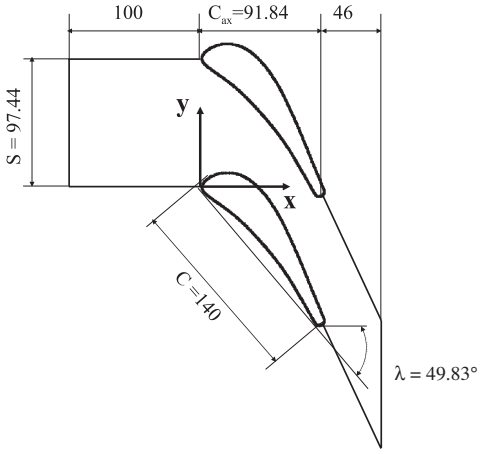

Fig. 1. Cascade dimensions (mm).

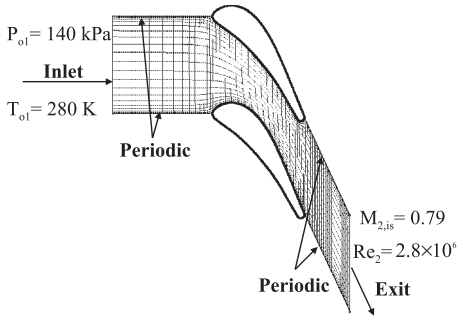

Fig. 2. Computational grid and boundary conditions.

2.2. Numerical scheme

Calculations were carried out using a locally developed structured single-block code, where Navier-Stokes equations were discretized by a cell vertex method. In this code, the lower upper symmetric Gauss Seidel (LUSGS) was used along with a dual-time method in order to obtain time accurate results for unsteady calculations. In addition, the AUSM scheme with E-fix was used to calculate inviscid numerical fluxes, where a second-order accuracy was achieved by the MUSCL scheme with the Van Albada flux limiter. On the other hand, the viscous fluxes were calculated by central differencing.

2.3. Grid and boundary conditions

Figure 2 shows the H-type grid and flow conditions used in the present calculation. The grid has 518 × 150 × 3 grid points in streamwise, pitchwise, and spanwise directions, respectively, with a total of 233,100 grid points. The minimum size of the grid is 0.001 mm. Every ninth line in the streamwise direction and every seventh line in the pitchwise direction are shown in Fig. 2.

The inlet boundary conditions are also in Fig. 2. Both total pressure ($P_{o1} = 140$ kPa) and total temperature ($T_{o1} = 280$ K) are imposed, but the static pressure ($p_2 = 92{,}755$ Pa) is imposed at the exit. In actual simulation, inlet and exit boundary conditions were calculated using the characteristics method.

2.4. Turbulence Model

The DES[20] method was adopted as the turbulence model. It is a hybrid scheme, working as a Reynolds Average Navier-Stokes (RANS) model near the wall and as a Large Eddy Simulation (LES) model away from the wall. Unlike RANS models, DES can provide more accurate results for unsteady flows. Moreover, unlike LES, DES does not require a very fine grid near the wall.

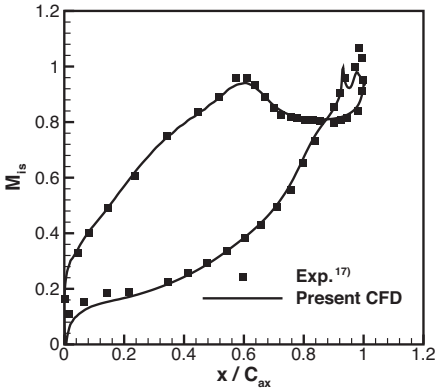

Fig. 3. Isentropic Mach number distribution.

3. Results and Discussion

3.1. Velocity distribution along blade surface

Figure 3 shows the distribution of time-averaged isentropic Mach number (M_{is}) around the blade along with the experimental data.[17] The present numerical result shows good agreement with the experimental data.

The flow is accelerated monotonously along the pressure surface until reaching the throat at the trailing edge. Along the suction surface, it has three phases: accelerated, decelerated, and constant flow. On the suction surface, flow is accelerated up to the throat ($x/C_{ax} = 0.61$), and is then decelerated due to the adverse pressure gradient in the diverging region of the cascade ($0.61 \leq x/C_{ax} \leq 0.75$). There is an isentropic Mach number plateau region at the straight suction surface from $x/C_{ax} = 0.75$ to the beginning of the trailing edge circle.

3.2. Distributions of time-average pressure in trailing edge region

Both time-averaged numerical and experimental[17] pressure distributions, normalized by the inlet total pressure (P_{o1}), along the circular trailing edge surface are shown in Fig. 4. The abscissa S represents the length along the circular trailing edge surface where the negative sign refers to the direction from the trailing edge ($S = 0$) toward the pressure surface, and the positive sign refers toward the suction surface. In this figure, D is the trailing edge thickness.

The experimental and numerical pressure results have good qualitative agreement, but there are some differences that might be caused by several factors such as the effects of grid and three-dimensionality. The numerical non-uniform pressure distribution along the trailing edge surface confirms the experimental data[17] and is different from the uniform pressure distribution observed experimentally by Cicatelli and Sieverding[14] and confirmed numerically by Sondak and Dorney[15] and Cicalelli et al.[16] at low Mach

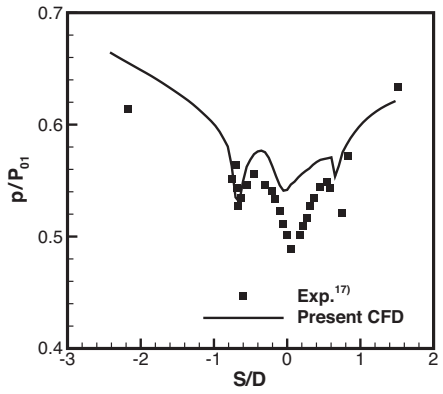

Fig. 4. Distributions of time-average pressure along trailing edge.

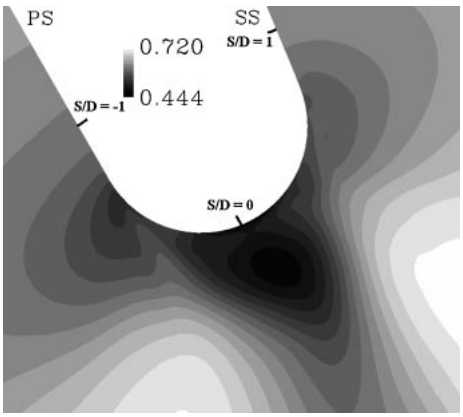

Fig. 5. Contours of time-averaged non-dimensional pressure near trailing edge; PS: pressure side; SS: suction side.

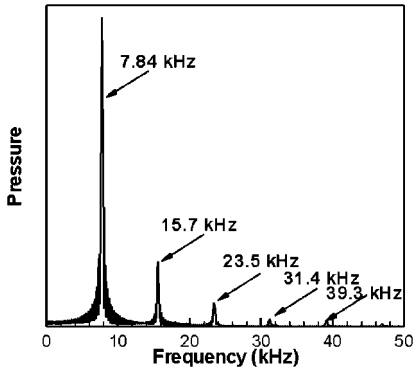

Fig. 6. Pressure spectra at $S/D = -0.65$.

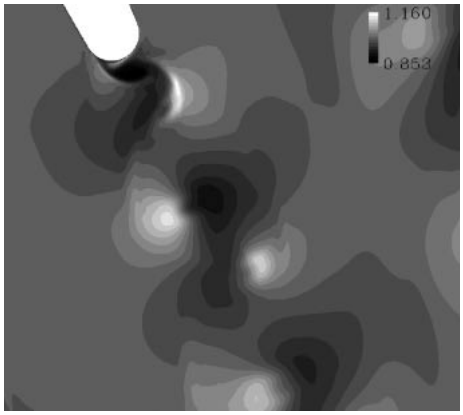

Fig. 7. Instantaneous non-dimensional total temperature contours.

number. El-Gendi et al.[21] showed that this non-uniform pressure distribution results from highly unsteady pressure fluctuations caused by vortex formation close to the trailing edge at this high Mach number, $M_{2is} = 0.79$. According to our unpublished data, RANS models, such as Baldwin-Lomax and Spalart-Allmaras turbulence models, have damped unsteady phenomena, which has been confirmed by Breuer et al.[22] for a flat plate and Schmidt et al.[23] for an airfoil. Therefore, they cannot capture this non-uniform pressure distribution. Moreover, steady calculation using DES also cannot capture this distribution.

Time-average pressure contours are shown in Fig. 5. There are three pressure minima, two next to the beginning of the trailing edge ($S/D = \pm 0.75$) at $S/D = \pm 0.65$ and a third at $S/D = 0$. The pressure increases gradually in the outward direction of the two minima at $S/D = \pm 0.65$. On the other hand, downstream of the third minima at $S/D = 0$, there is an almost circular region of low pressure resulting from vortices formation. The pressure increases gradually in the outward direction of this circle.

3.3. Vortex shedding frequency

Spectral analysis was made for the pressure fluctuations at $S/D = -0.65$ (Fig. 6). There is a predominant vortex shedding frequency at 7.84 kHz, showing reasonable agreement with the experimentally obtained frequency[4] of 7.6 kHz and deviating from it by 3.16%. The pressure trace at this point is almost sinusoidal.[21]

3.4. Energy separation phenomenon

In the cylinder wake, Kurosaka et al.[2] confirmed that this phenomenon is caused by the vortex street and proposed many theoretical models for its interpretation. Based on the numerical results from this study, we consider the phenomenon in more depth and clarify its cause.

Contours of the total temperature normalized by inlet value are shown in Fig. 7. The total temperature at the hot spots reaches $1.16T_{o1}$, which is 44.8 K higher than the inlet total temperature. On the other hand, at the cold spots, it decreases to $0.853T_{o1}$, which is 41.16 K lower.

Figure 8 shows instantaneous non-dimensional vorticity contours. The formation of the vortex is so close to the trailing edge that the pressure distribution at the trailing edge is non-uniform (Figs. 4, 5). From comparison of Fig. 7 and Fig. 8, the hot spots are at the outside edge of the vortex toward the potential flow, while the cold spots are at the inside edge of the vortex toward the wake center, whether the vortex is shed from the pressure or suction surface.

Kurosaka and Sundaram[24] showed that the particles' pathlines are trochoidal in the wake of a cylinder. A similar pattern is also observed in the present turbine wake (see Fig. 9). Here we consider two directions: tangential and transverse directions. The tangential direction is tangent to the camber line at the trailing edge, which takes an angle

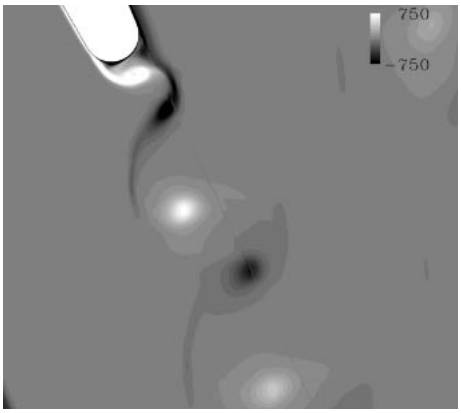

Fig. 8. Contours of instantaneous non-dimensional vorticity.

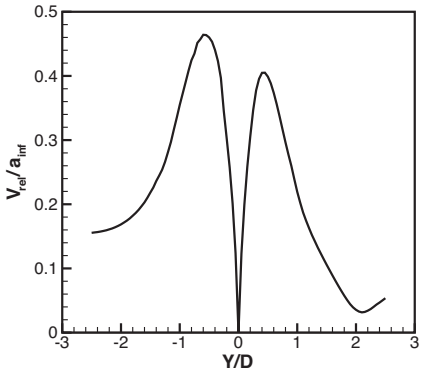

Fig. 10. Distribution of relative velocity across vortex.

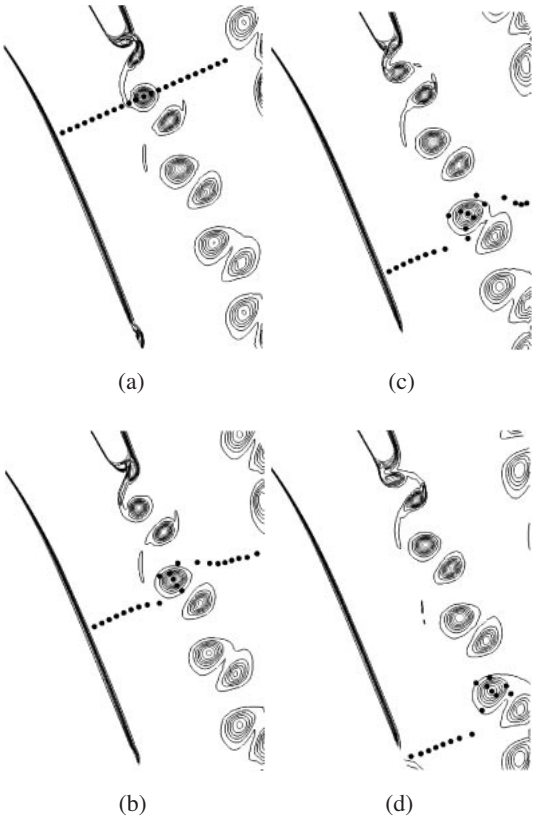

Fig. 9. Particles movement and vortex motion (entropy contours).

of 66° from the axial direction. On the other hand, the transverse direction is normal to the tangential direction. In Fig. 9(a), particles in the transverse direction across the vortex center are marked. With time, particles inside the vortex rotated and formed curtate pathlines, because the convective velocity is greater than the rotational velocity (Kurosaka et al.).[2)]

Although each particle in the vortex has a different velocity direction or magnitude or both (as shown later), the vortex as a whole moves a little slower than the potential flow outside the vortex.

From this trochoidal pathline we believe that velocity, which is a superposition of convective and rotational velocities, is the main reason for energy separation. To verify this hypothesis, vortex with marked particles in Fig. 9(a) is examined. Some flow properties were calculated in the tangential and transverse directions.

Converting the view from the stationary frame to the vortex's convective velocity frame obtains the relative velocity (V_{rel}) of the vortex in the transverse direction (Fig. 10). The vortex is similar to a Rankine vortex. The speed of sound, a_{inf}, was calculated from inlet and exit boundary conditions and isentropic relations.

$$T_{\mathrm{inf}} = T_{\mathrm{o1}}\left(1 + \frac{\gamma - 1}{2} M_{2,\mathrm{is}}^2\right)^{-1}$$

$$a_{\mathrm{inf}} = \sqrt{\gamma R T_{\mathrm{inf}}}$$

The superposition process of velocity is shown in Fig. 11 in the transverse and tangential direction. Dashes, dots, and solid arrows represent the convective, rotational, and resultant velocities, respectively. The small dashed, solid, and large dash circles represent points in the solid rotation, the location at the highest rotational velocity, and points in the free vortex region, respectively. The abscissa and ordinate represent tangential and transverse directions, respectively. The axes origin was taken at the vortex center.

Figure 12(a) shows some flow properties in the transverse direction. The entropy distribution indicates that the maximum loss at the vortex center and the vortex covers slightly a distance greater than twice the trailing edge diameter. Due to dissipation and convection, the static temperature behaviour is unclear; generally, there is a slightly higher value at the vortex center and small variations along the vortex. Both static pressure and density have similar trends with minimum values at the vortex's center, increasing outward.

The velocity distribution is explained by referring to Fig. 11. In the upper part of the vertical line in Fig. 11, which corresponds to $Y/D \leq 0$ in Fig. 12(a), the direction of convective velocity coincides with the direction of the rotational velocity of the vortex.

Toward the vortex center, the resultant velocity increases gradually due to the increase in rotational velocity until its maximum is reached (solid circle in Fig. 11, and at $Y/D \simeq -0.4$ in Fig. 12(a)). The dimensionless velocity, V/a_{inf}, exceeds 1.1 near the vortex centerline. Unfortunately, Sieverding et al.[4,17)] didn't carry out instantaneous velocity

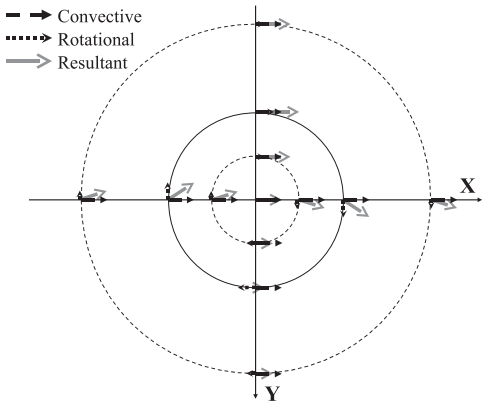

Fig. 11. Superposition of velocity.

measurements to confirm this observation. However, Armstrong et al.[25] made instantaneous velocity measurement across the vortex center line in the transverse direction of the cylinder wake at low subsonic Mach number. There is a similar trend between their experimental data and our calculations, in terms of instantaneous velocity distribution. Closer to the vortex center, the resultant velocity is reduced due to solid rotation. Moving again outward (lower part of vertical line in Fig. 11, and $Y/D > 0$ in Fig. 12(a)), the direction of rotational and convective velocities becomes opposite. Although the rotational velocity increases, the resultant velocity continues to decrease until it reaches its minimum at the edge of the vortex core, where the rotational velocity is maximum (solid circle in Fig. 11 and at $Y/D \simeq 0.4$ in Fig. 12(a)). Moving further outward, the rotational velocity decreases, so resultant velocity increases.

This velocity behavior has a substantial impact on the total temperature distribution and causes the energy separation. Also, similarly, the velocity distribution affects both total density and pressure distributions. The static values of density and pressure affect their total values more than that of temperature.

Figure 12(b) shows the flow properties in the tangential direction, which are the same as those in the transverse direction. The entropy distribution has its maximum value at the vortex center and decreases outward. The vortex width covers a distance slightly shorter than twice the trailing edge diameter, indicating that the vortex is not strictly a circle, because, in the transverse direction, the vortex covers a distance slightly higher than twice the trailing edge diameter. Smaller entropy peaks on both sides of the investigated vortex result from neighboring vortices. Neighboring vortices affect not only entropy but also other flow properties shown in Fig. 12(b). The trend of both static temperature and pressure as well as density is similar to that of the transverse direction.

Also, in the tangential direction, the velocity distribution can be interpreted with the aid of Fig. 11. The left-hand side of the horizontal line in Fig. 11 represents approximately the region where $-1 \leq X/D \leq 0$. The rotational velocity is orthogonal to convective velocity. Toward the vortex center, the rotational velocity increases and hence the resultant velocity increases until reaching the maximum values at the start of solid body rotation (solid line circle Fig. 11, and $\simeq -0.4$ Fig. 12(b)). Note that the resultant velocity's maximum in the transverse direction is higher than that in the tangential direction: in the transverse direction, both velocities coincided whereas, they are orthogonal in the tangential direction. In solid body rotation, both velocities decrease until the resultant velocity reaches its convective component. Moving outward again, on the right-hand side in Fig. 11, which represents approximately $0 \leq X/D \leq 1$, the rotational velocity has an angle -90° to the convective velocity. The resultant velocity has a similar trend to $-1 \leq X/D \leq 0$ with negative angles. However, the effect of the angle sign does not appear in the resultant velocity in Fig. 12(b) because of absolute values, i.e., the ordinate at $X/D = 0$ works as a mirror (Fig. 12(b)). Like the transverse direction, the velocity affects both the total temperature

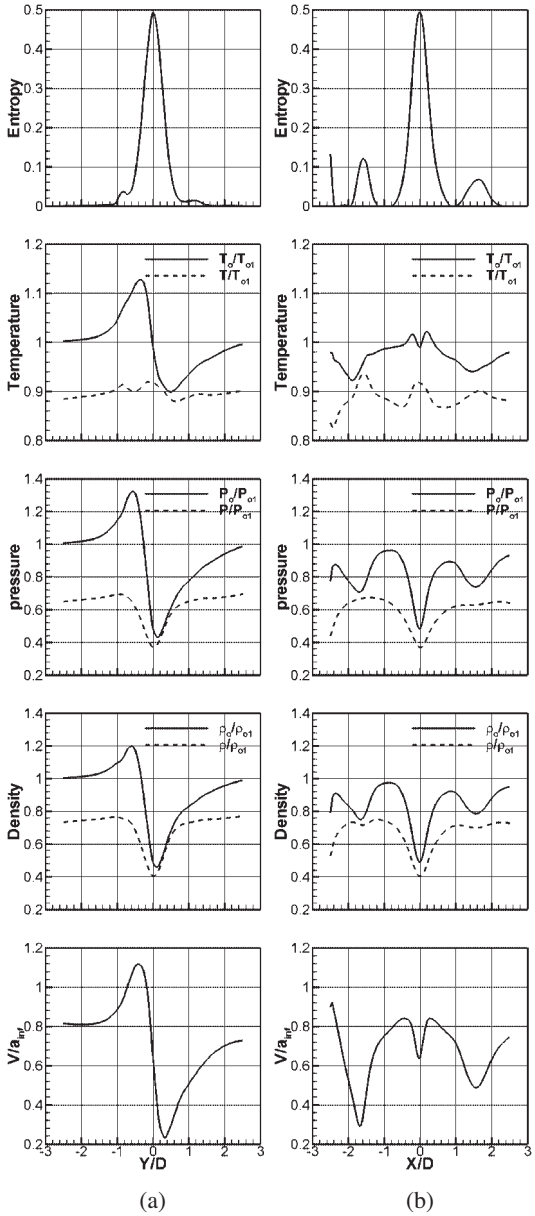

Fig. 12. Flow properties along: (a) transverse direction; (b) tangential direction.

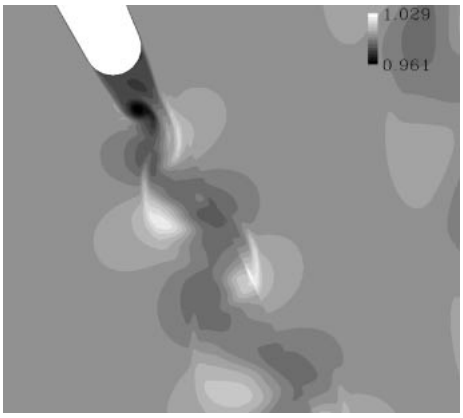

Fig. 13. Instantaneous non-dimensional total temperature contours at $M_{2,is} = 0.4$.

distribution and the total pressure and density distributions. In addition, there is slight total temperature variation along the X-axis in the inviscid region of the vortex, which is different from the kinematical hypothesis of Kurosaka et al.[2] and Eckert.[8]

Generally, in the regions with high resultant velocities, the total temperature, pressure, and density become high (hot spots). On the other hand, in the region with low resultant velocity, they become low (cold spots). Hence energy separation occurs.

3.5. Compressibility effect

To study the effect of compressibility on the energy separation, the flow was simulated numerically at $M_{2,is} = 0.4$ and $Re_2 = 2 \times 10^6$. Figure 13 shows the instantaneous total temperature contours normalized by inlet value, T_o/T_{o1}, at $M_{2,is} = 0.4$. The dimensionless total temperature at the hot spots reaches 1.029, which is lower by 0.131 than T_o/T_{o1} at $M_{2,is} = 0.79$ (Fig. 7). On the other hand, at the cold spots, it decreases to 0.961, which is higher by 0.108 than at $M_{2,is} = 0.79$ (Fig. 7). At $M_{2,is} = 0.4$, the energy separation maintains the same features as at $M_{2,is} = 0.79$ with a narrower range. In subsonic flows, the higher the Mach number, the stronger the energy separation.

3.6. Eckert-Weise effect

On the time-average basis, the energy separation is termed the Eckert-Weise effect. Figure 14 shows the coordinate system used in the wake. The X-axis is tangential to the camber line at the trailing edge and forms 66° to cascade axial direction. The Y-axis represents the transverse direction and is normal to X. The origin of the axes was taken at the trailing edge. The calculated locations of the time-average total temperature are shown in Fig. 14 as transverse lines.

The numerical time-average total temperature distributions at several transverse locations are shown in Fig. 15 along with experimental data[4] at $X/D = 2.5$. Both numerical results and experimental data have a similar trend where the total temperature has low values at the wake middle and high values at the wake border and approaching its inlet value in the potential flow region outside the wake. At $X/D = 2.5$, the discrepancy between the experimental and

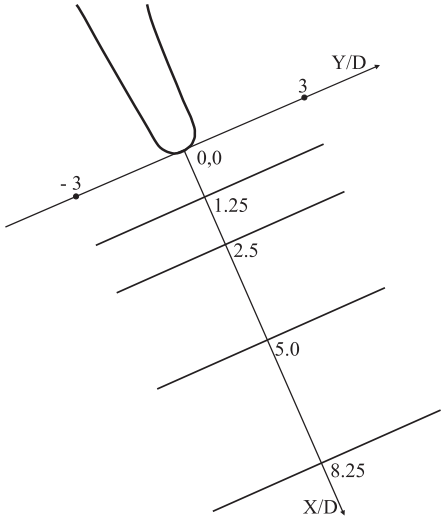

Fig. 14. Wake coordinates.

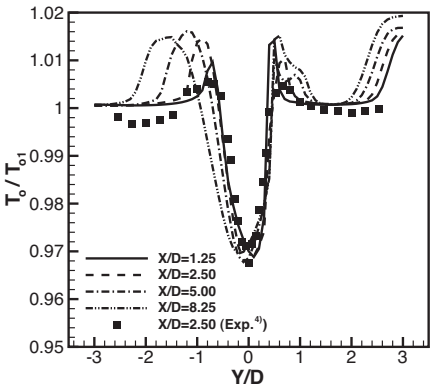

Fig. 15. Time-average total temperature distribution in wake.

numerical results at $Y/D < -1.5$ falls within the probe accuracy.[4] On the other hand, this discrepancy at $Y/D \pm \simeq 1$ and at $Y/D > 2.5$ (resulting from wake effect of neighboring blade) may be attributed to a 3 D effect or incomplete wake formation due to grid skewness and resolution.

Because the vortex is still in the formation phase at $X/D = 1.25$ (Fig. 8), the Eckert-Weise effect at this location is lower than that at $X/D = 2.5$. Moving farther downstream to the dissipation phase (Fig. 8), the Eckert-Weise effect is reduced and widened.

4. Conclusion

We numerically simulated flow in a turbine cascade at an exit isentropic Mach number of 0.79, and a Reynolds number of 2.8×10^6. The main results are as follows:

1. The numerical results have good agreement with experimental data with some discrepancies.
2. The existence of a non-uniform pressure distribution around the trailing edge at rather high Mach number has been confirmed numerically.
3. Combination of the convective and rotational velocities of the vortex is the main cause of energy separa-

tion. Hence, both total pressure and total density have a similar trend to total temperature in the wake. In addition, energy separation becomes stronger with increasing Mach number, and the vortex formation and dissipation affect the Eckert-Weise effect.

Acknowledgments

The first author's doctoral program is supported by the Egyptian Ministry of Higher Education. This work was supported by a Grant-in-Aid for 21st Century COE "Frontiers of Computational Science." We would like to thank Prof. Sieverding who was kind enough to supply us with the blade coordinates. We are also grateful to Dr. A. Hashimoto, Dr. M. Jones, Prof. I. Men'shov, and M. El-Ghandour for their interesting discussions and fruitful advice.

References

1) Denton, J. D.: Loss Mechanisms in Turbomachines, *ASME J. Turbomach.*, **115** (1993), pp. 621–656.
2) Kurosaka, M., Gertz, J. B., Graham, J. E., Goodman, J. R., Sundaram, P., Riner, W. C., Kuroda, H. and Hankey, W. L.: Energy Separation in a Vortex Street, *J. Fluid Mech.*, **178** (1987), pp. 1–29.
3) Carscallen, W. E., Currie, T. C., Hogg, S. I. and Gostelow, J. P.: Measurement and Computation of Energy Separation in the Vortical Wake Flow of a Turbine Nozzle Cascade, *ASME, J. Turbomach.*, **121** (1999), pp. 703–708.
4) Sieverding, C. H., Ottolia, D., Bagner, C., Comadoro, A., Brouckaert, J. F. and Desse, J.: Unsteady Turbine Blade Wake Characteristics, *ASME, J. Turbomach.*, **126** (2004), pp. 551–559.
5) Goldstein, R. J. and Kularni, K. S.: Energy Separation in the Wake of a Cylinder, *ASME, J. Heat Transfer*, **130** (2008), pp. 061703-1–9.
6) Goldstein, R. J. and He, B.: Energy Separation and Acoustic Interaction in Flow Across a Circular Cylinder, *ASME, J. Heat Transfer*, **123** (2001), pp. 682–687.
7) Ng, W. F. and Chakroun, W. M.: Time-Resolved Measurements of Total Temperature and Pressure in the Vortex Street behind a Cylinder, *Phys. Fluids A*, **2** (1990), pp. 971–978.
8) Eckert, E. R. G.: Cross Transport of Energy in Fluid Streams, *Wärme- und Stoffübertragung*, **21** (1987), pp. 73–81.
9) Eckert, E. R. G.: Energy Separation in Fluid Streams, *Int. Comm. Heat Mass Transfer*, **13** (1986), pp. 127–143.
10) O'Callaghan, J. J. and Kurosaka, M.: Vortex-Induced Energy Separation in Shear Flows, *AIAA J.*, **31** (1993), pp. 1157–1159.
11) van Oudheusden, B. W.: Energy Separation in Steady Separated Wake Flow, *ASME, J. Fluids Eng.*, **127** (2005), pp. 611–614.
12) Cicatelli, G. and Sieverding, C. H.: A Review of The Research on Unsteady Turbine Blade Wake Characteristics, Tech. Rep., AGARD-CP-571, Loss Mechanisms and Unsteady Flows in Turbomachines, Paper 6 (1996), pp. 6-1–6-13.
13) Desse, J.: Effect of Time-Varying Wake Flow Characteristics behind Flat Plates, *AIAA J.*, **36** (1998), pp. 2036–2043.
14) Cicatelli, G. and Sieverding, C. H.: The Effect of Vortex Shedding on the Unsteady Pressure Distribution around the Trailing Edge of a Turbine Blade, *ASME J. Turbomach.*, **119** (1997), pp. 810–819.
15) Sondak, D. L. and Dorney, D. J.: Vortex Shedding in A Turbine Cascade, AIAA-1998-3573; AIAA/ASME/SAE/ASEE Joint Propulsion Conference and Exhibit, 34th, Cleveland, OH, 1998.
16) Manna, M., Mulas, M. and Cicatelli, G.: Vortex Shedding behind a Blunt Trailing Edge Turbine Blade, *Int. J. Turbo Jet Engine*, **14** (1997), pp. 145–157.
17) Sieverding, C. H., Richard, H. and Desse, J.: Turbine Blade Trailing Edge Flow Characteristics at High Subsonic Outlet Mach Number, *ASME, J. Turbomach.*, **125** (2003), pp. 298–309.
18) Sieverding, C. S., Cicatelli, G., Desse, J. M., Meinke, M. and Zunino, P.: Experimental and Numerical Investigation of Time Varying Wakes behind Turbine Blades, *Notes Numer. Fluid Mech., Vieweg*, **67** (1999).
19) Mensink, C.: Numerical Prediction of Periodic Vortex Shedding in Subsonic and Transonic Turbine Cascade Flows, *Int. J. Numer. Meth. Fluids*, **22** (1996), pp. 881–897.
20) Wilcox, D. C.: *Turbulence Modeling for CFD*, DWC Industries, Inc., California, USA, 2006.
21) El-Gendi, M., Ibrahim, M. K., Mori, K. and Nakamura, Y.: Numerical Simulation of Trailing Edge Vortex Shedding in a High Subsonic Turbine Cascade, Proceedings of 2007 JSASS-KSAS Joint International Symposium on Aerospace Engineering, 2007, pp. 8–11.
22) Breuer, M., Jovicic, N. and Mazaev, K.: Comparison of DES, RANS, and LES for the Separated Flow around a Flat Plate at High Incidence, *Int. J. Numer. Meth. Fluids*, **41** (2003), pp. 357–388.
23) Schmidt, S. and Thiele, F.: Detached Eddy Simulation of Flow around A-Airfoil, *Flow, Turbul. Combust.*, **71** (2003), pp. 261–278.
24) Kurosaka, M. and Sundaram, P.: Illustrative Examples of Streaklines in Unsteady Vortices: Interpretational Difficulties Revisited, *Phys. Fluid*, **29** (1986), pp. 3474–3477.
25) Armstrong, B., Barnes, F. H. and Grant, I.: A Comparison of the Structure of the Wake behind a Circular Cylinder in a Steady Flow with that in a Perturbed Flow, *Phys. Fluid*, **30** (1987), pp. 19–26.